CHAPTER V

SYNTHESIS OF Fe-Ti-MCM-48 FROM SILATRANE PRECURSOR VIA SOL-GEL PROCESS AND ITS HYDROTHERMAL STABILITY

5.1 Abstract

A series of bimetallic Fe-Ti-MCM-48 materials were successfully synthesized via sol-gel method using cetyltrimethylammonium bromide (CTAB) as a template, silatrane, iron (III) chloride, and titanium (IV) isopropoxide as silica, iron, and titanium sources, respectively. Scanning electron microscopy (SEM) showed the truncated octahedron morphology of Fe-Ti-MCM-48. X-ray diffraction (XRD) patterns showed well-defined order cubic mesoporous structures. X-ray fluorescence (XRF) revealed the total metal content of the final product. UV-visible absorption spectra confirmed that both iron (Fe^{3+}) and cerium (Ti^{4+}) species highly dispersed in the framework. While N_2 adsorption/desorption measurements indicated that high specific surface area. As metal content increased, the mesoporous order and surface area decreased. The synthesized Fe-Ti-MCM-48 with 0.01Fe/Si and 0.01Ti/Si ratio still retained a cubic structure after hydrothermal treatment at 100 °C for 72 h.

5.2 Introduction

The cubic MCM-48, a main member in M41S family discovered by Mobil group [1], performs three-dimensional pore channel that can avoid pore blocking and provide faster reactants diffusion than one-dimensional pore system of MCM-41 [2-4]. Due to tunable pore diameter, well-defined structure, and large surface area, MCM-48 has been used in many applications, such as catalyst, catalyst support, adsorbent, sensor, and template, for the synthesis of advanced nanostructures [5-9]. However, pure silica porous material is inert for catalytic applications because of its lack of active sites. In order to create the active sites, the metal ions such as Fe, Ce, Cr, V and Ti have been used to modify the MCM-48 silica framework [10-12]. Among the metals, iron containing mesoporous silica gave a good catalytic performance for the selective oxidation processes, such as Friedel–Crafts [13], styrene epoxidation [14], Fischer-Tropsch [15], and phenol hydroxylation [16-17]. Titanium substituted mesoporous silicates also have excellent ability in photocatalytic activity [18-19], styrene epoxidation [14], toluene oxidation [20], and phenol hydroxylation [21]. However, in this case the structure of Ti-MCM-41 collapsed under mild conditions for phenol hydroxylation with H_2O_2 [21]. Xiao et al. [22] found that an ordered mesoporous titanasilicate retained the structure after treatment in boiling water for 120 h. Chen et al. [23] studied Ti-substituted MCM-41 with various treatments and reported that the structural stability can be improved by Ti incorporation. Galacho et al. [24] also demonstrated that Ti-MCM-41 maintained the structure after 12 h in boiling water and the hydrothermal stability of titanium substituted samples increased as increase titanium content. The incorporation multi-components of metal atoms can modify silica surface that might create new properties and improve catalytic activity, selectivity, acidity, hydrophobicity, and stability of the single-component catalysts [25-27]. Wang et al. [27] studied the liquid-phase epoxidation of styrene, and found that bimetallic Zr-Ti-MCM-41 had high catalytic activity and selectivity over single metal Zr-MCM-41 or Ti-MCM-41. MCM-41 incorporated with copper and titanium was first synthesized by Kong et al. [28] who indicated that Cu-Ti-MCM-41 had relatively high thermal stability. Wang et al. [29] found that Ti-containing Cr-modified MCM-48 photocatalysts had the

photocatalytic performance for decomposition of H_2S under visible light with 92% efficiency for H_2S removal. The reduction of NO with NH_3 using Fe-Mo-SBA-15 as a catalyst performed higher catalytic activity than monometallic modified SBA-15 [30]. Bimetallic V-Fe-SBA-15 [31] and Ce-Fe-SBA-15 [32] were used for hydroxylation of phenol. An appropriate metals mol ratio (V/Fe and Ce/Fe) in SBA-15 would enhance the catalytic performance [31-32]. Popova et al. [33] reported that titanium- and iron- modified MCM-41 achieved higher catalytic activity, compared to monosubstituted material for toluene oxidation. Fe-Ti incorporated SBA-15 and MCM-41 were synthesized for hydroxylation of styrene with H_2O_2 [26] and the conversion of styrene was controlled by metal content. Iron and titanium have the ability to catalyze in the same reactions of phenol hydroxylation [16-17, 21] and styrene epoxidation [14], incorporation of these two metal atoms into mesoporous silica might thus enhance the catalytic activity over the monometallic material. Up until now, there are few published reports on bimetallic MCM-48 due to difficulty of preparation [29].

In this work, Fe-Ti-MCM-48 with different Fe/Si and Ti/Si mol ratios was synthesized under hydrothermal condition via sol-gel process. The hydrothermal stability was also studied to determine the destruction of catalyst structure that might decrease the catalytic ability.

5.3 Experimental

5.3.1 Materials

Fumed silica (99.8%, SiO_2) and iron (III) chloride hexahydrate ($FeCl_3 \cdot 6H_2O$) from Sigma-Aldich, titanium (IV) isopropoxide ($Ti(OCH(CH_3)_2)_4$) from Acros Organics, cetyltrimethylammonium bromide (CTAB) from Fluka, ethylene glycol (EG) from J.T. Baker, triethanolamine (TEA) from QREC, acetronitrile and sodium hydroxide (NaOH) from Labscan were used without purification.

5.3.2 Preparation of Bimetallic materials

xFe-yTi-MCM-48 were synthesized, following Wongkasemjit's method [34]. The molar ratio composition of the obtained gel was $1.0SiO_2:0.3CTAB:0.5NaOH:62.0H_2O:x$Fe:$y$Ti, where $0.01 \leq x$, $y \leq 0.09$. Firstly, $FeCl_3 \cdot 6H_2O$ was dissolved in distilled water, followed by adding 2 M NaOH and CTAB. The mixture was continuously stirred and slightly heated at 50 °C. The desired amount of silatrane, prepared according to the method reported in the literature [35], was added into the solution. Then the required amount of $Ti(OCH(CH_3)_2)_4$ was added dropwise into the mixture and stirred for 1 h. The resulting mixture was transferred into a teflon-lined stainless steel vessel and autoclaved at 140 °C for 16 h. The powder product was washed and filtered with distilled water. After drying, the organic template was removed by calcination at 550 °C for 6 h with a heating rate of 0.5 °C/min. Pure MCM-48, Fe-MCM-48 and Ti-MCM-48 were prepared using the same procedure.

5.3.3 Characterization

The powder X-ray diffraction (XRD) patterns were recorded on a Rigaku X-ray diffractometer with CuKα radiation over the range of $2\theta = 2$-$6°$. N_2 adsorption and desorption isotherms were measured using by a Quantasorb JR instrument using the Brunauer–Emmett–Teller (BET) method. The diffuse reflectance UV-visible (DRUV-vis) analysis of samples was carried out by a Shimadzu UV-2550. X-ray fluorescence (XRF) was observed on a PANalytical AXIOS PW 4400. The morphology was determined by using field emission- scanning electron microscope (FE-SEM) with a Hitachi S-4800 model. Transmission electron microscopy (TEM) was applied to investigate the microstructure using a JEOL JEM-2010.

5.3.4 Hydrothermal stability test

Following the method by Jiang et al. [36], 0.1 g of calcined sample was added into a teflon-lined stainless steel vessel containing 50 ml distilled water and treated at 100 °C for different times (12, 24, 36, 48, and 72 h). The sample was

recovered by filtration and dried overnight at ambient temperature. The treatment product was characterized by XRD.

5.4 Results and Discussion

5.4.1 XRD

Figure 5.1 shows the XRD patterns of MCM-48, Fe-MCM-48, Ti-MCM-48 and Fe-Ti-MCM-48. All samples exhibited the intense {211} peak and weak {220}, {420}, and {332} peaks which suggest the $Ia3d$ cubic phase of MCM-48 mesoporous materials [34]. Compared with pure MCM-48, XRD patterns of metal incorporated MCM-48 shifted slightly to a higher angle and a lower d-spacing with a decrease in the peak strength, implying that the different sizes of metal, the radii of Fe^{3+} (Paulling radius = 64 pm) and Ti^{4+} (Paulling radius = 60 pm) were larger than Si^{4+} (Paulling radius = 42 pm), causing the geometric distortion from the ideal tetrahedral coordination [37]. The synthesis of Fe-MCM-48 with Fe/Si ratio beyond 0.01 was not successful due to the imbalance of charge matching, as explained in elsewhere [38]. Therefore, bimetallic xFe-yTi-MCM-48 only when x = 0.01 and $0.01 \leq y \leq 0.09$ obtained the cubic structure. On the other hand, Ti-MCM-48 was successfully synthesized using $Ti(OCH(CH_3)_2)_4$ as titanium precursor that generated isopropoxide anion. According to the surfactant-packing parameter (g); $g = V/a_0l$ where V is the volume of the hydrocarbon chain of surfactant monomer, a_0 is the effective head group area of the cationic ammonium and l is the apparent length of the hydrophobic tail of the surfactant, the hydrophobic part of isopropoxide anion combined with the hydrocarbon region of the surfactant to result in an increase in V [39]. Thus, following the surfactant-packing parameter equation, a large g value was also obtained as well. Besides, Mahoney et al. [40] suggested that the cubic formation was favorable of high curvature surface and large g because of the imbalance of charge distribution. Between titanium and iron precursors, isoproproxide anion was more effective precursor than chloride anion to form MCM-48. In addition, it was also found that the peak shifted to lower angle as the content of titanium increased for Ti-MCM-48. The reason was explained by Gao et al. [31]

that more titanium incorporated and large size of titanium would enlarge the structure [31]. The XRD pattern clearly exhibited that bimetallic Fe-Ti-MCM-48 can be prepared at various Ti contents with 0.01 Fe/Si. The change in the relative intensities and the obvious shift to higher angle of the bimetallic products suggested that TiO_2 nanocrystal was present on the internal pore wall of MCM-48 [41].The wide angle XRD pattern of Fe-Ti-MCM-48 is shown in Fig. 5.2. The broad peak at 23° referred to the amorphous SiO_2. The characteristic peak of TiO_2 was obscurely seen since the titania is in the amorphous phase which also presented in TiO_2/SiO_2 with 450-550°C calcined temperature [42] and trace amount of titanium was incorporated in MCM-48 that showed the same broad peak as TiO_2-SiO_2 gel composite with less than 10%wt TiO_2 loading [43].
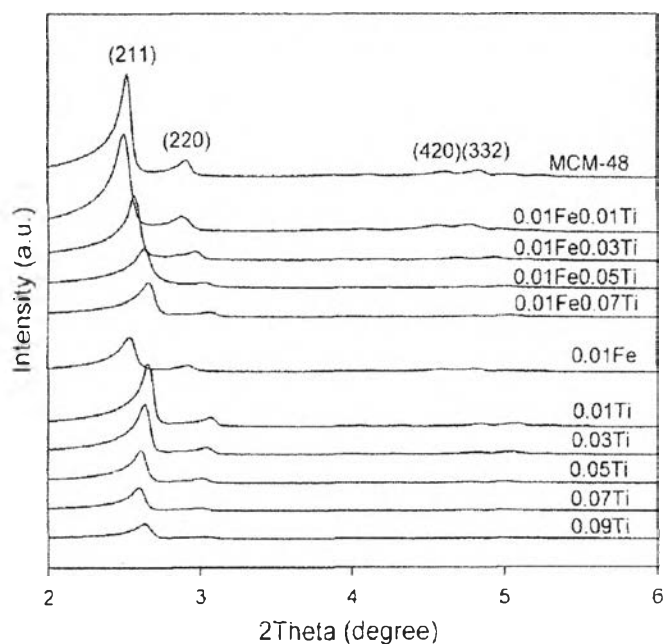
Figure 5.1 Small angle XRD patterns of MCM-48, Fe-MCM-48, Ti-MCM-48, and Fe-Ti-MCM-48.
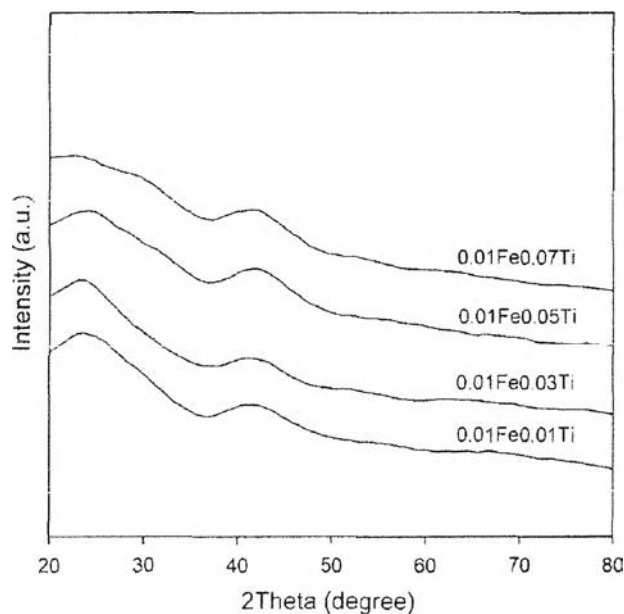
Figure 5.2 Wide angle XRD patterns of 0.01Fe0.01Ti-MCM-48, 0.01Fe0.03Ti-MCM-48, 0.01Fe0.05Ti-MCM-48 and 0.01Fe0.07Ti-MCM-48.

5.2.2 N₂ adsorption-desorption

The isotherms and the pore size distribution of MCM-48 and Fe-Ti-MCM-48 samples are shown in Fig. 5.3. All adsorption isotherms were type IV, typical of mesoporous materials that exhibit the sharp capillary condensation steps at relative pressure of $0.20 \leq p/p_0 \leq 0.35$. As a result, the capillary condensation of bimetallic MCM-48 became less steep when the amount of Ti increased, indicating a broader pore size distribution. Thus, as more Ti incorporated into the structure, the structure was less ordered, as can be seen from the XRD patterns in Fig. 5.1. The structure parameters of the samples are given in Table 5.1. The average pore sizes of the obtained samples were 2–3 nm. Also, the uniform narrow pore size distribution was demonstrated.Fe-MCM-48 performed large pore volume and slim wall thickness similar to those reported by Das and co-workers [44]. All Ti-MCM-48 samples had higher wall thickness than siliceous MCM-48 due to the incorporation of Ti into

MCM-48 framework. The specific surface area of Ti-MCM-48 and Fe-Ti-MCM-48 decreased as the metal content increased since there was some destruction of the metallic MCM-48 in agreement with the XRD results [45]. Nevertheless, all samples resulted in high surface area.
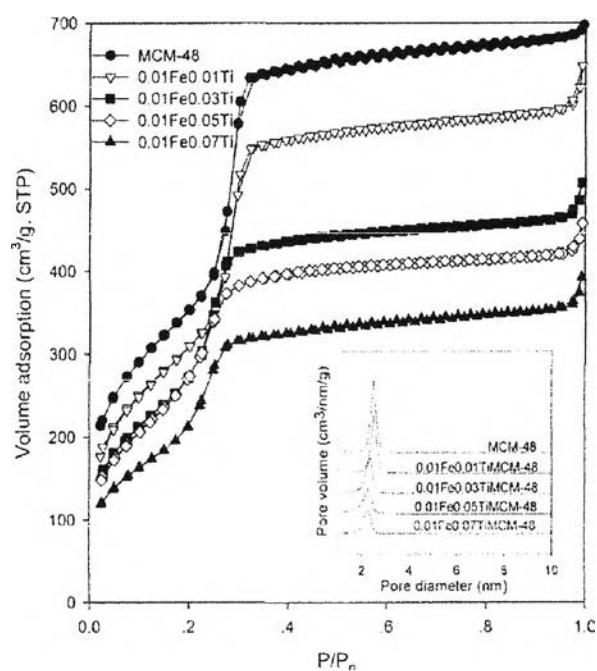

Figure 5.3 Nitrogen adsorption-desorption isotherms of MCM-48 and Fe-Ti-MCM-48.

5.4.3 DRUV

The DRUV spectra (Fig. 5.4a-b) were analyzed to characterize the coordination circumstance of metal ion coordination. There was no absorption band observed for MCM-48. For Fe-MCM-48 (Fig. 5.4a), a broad band between 200 and 350 nm centered at 220 nm, was assigned to the charge transfer transitions involving isolated Fe^{3+} in tetrahedral geometry [46]. Ti-MCM-48 in Fig. 5.4a also showed one intense peak at 210 nm which referred to the ligand metal charge transfer between O^{2-} and Ti^{4+} in tetrahedral framework coordination [47], and the intensity increased

as increasing the amount of Ti content. The Fe-Ti-MCM-48 samples exhibited a broad absorption at 200–300 nm, as shown in Fig. 5.4b, which attributed to the charge transfer transitions between tetrahedral oxygen ligand and the central Ti^{4+} and Fe^{3+} that overlapped at the same wavelength position. However, the presence of the band at around 500 nm demonstrated some M-O-M clusters existence of isolated Ti sites [26], corresponding to nanocrystalline TiO_2, which is in good agreement with XRD wide angle.
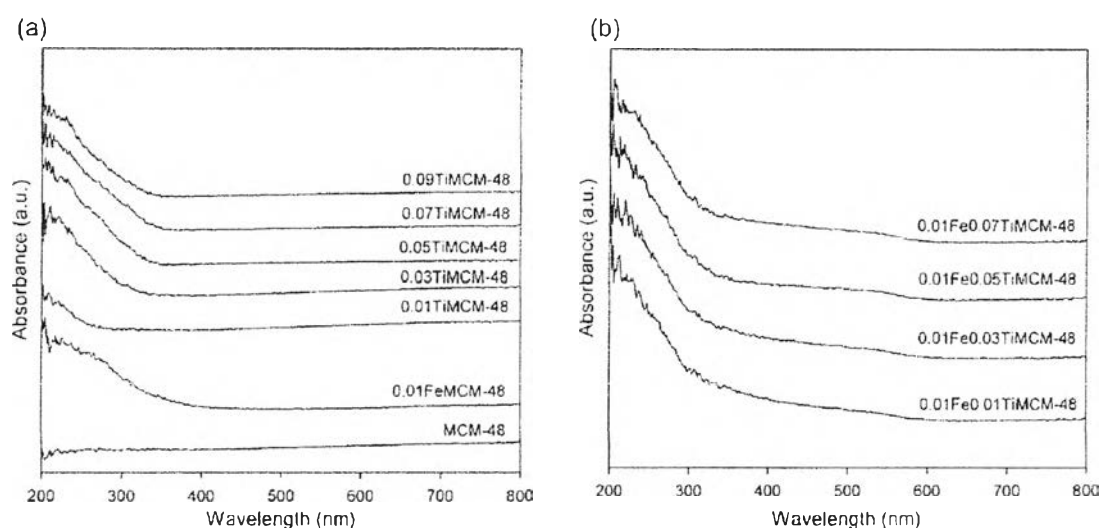
Figure 5.4 DRUV-vis spectra of samples: (a) MCM-48, Fe-MCM-48 and Ti-MCM-48; (b) Fe-Ti-MCM-48.

Table 5.2 shows the band gap energies of Fe-MCM-48 and Ti-MCM-48, calculated from UV-vis spectra (See appendices for calculation). The band gap energy of bimetallic Fe-Ti-MCM-48 could not be possible to identify due to the overlap of Ti^{4+} and Fe^{3+} peaks. 0.01Fe-MCM-48 exhibits the band gap value around 3.250 eV while the band gap of Ti-MCM-48 decreased with the red shift in adsorption band when increasing the Ti content. Serpone [51] and Oleksek et al.[52] also reported that the increase in the dopant concentration decreased the band gap, resulting in a narrow band gap materials and the easier excitation of electron in the valence band to the conduction band [53].

Table 5.1 Band gap energy of metal modified MCM-48

Materials	Wavelength (nm)	Band gap energy (eV)
0.01Fe-MCM-48	381.3	3.250
0.01Ti-MCM-48	280.0	4.426
0.03Ti-MCM-48	317.6	3.902
0.05Ti-MCM-48	352.5	3.516
0.07Ti-MCM-48	372.6	3.327
0.09Ti-MCM-48	373.8	3.316

5.4.4 XRF

The XRF results indicate the actual amounts of Fe and Ti introduced into MCM-48. The metal contents in the final product had lower amount than those in the gel, as shown in Table 5.1, due to the solubility of Fe and Ti precursors in the medium.

Table 5.2 Textural properties of MCM-48 and metal modified MCM-48

Sample	Fe/Si* (mole ratio)		Ti/Si* (mole ratio)		BET surface area (m^2/g)	pore volume (cm^3/g)	pore diameter (nm)	a_0 [a] (nm)	d_{211} (nm)	wall thickness [b] (nm)
	Gel	Product	Gel	Product						
MCM-48	0	0	0	0	1673	1.07	2.56	8.57	3.50	1.46
0.01Fe-MCM-48	0.01	0.004	0	0	1295	0.98	3.04	8.65	3.53	1.28
0.01Ti-MCM-48	0	0	0.01	0.003	1549	0.84	2.18	8.13	3.32	1.61
0.03Ti-MCM-48	0	0	0.03	0.015	1201	0.64	2.12	8.18	3.34	1.63
0.05Ti-MCM-48	0	0	0.05	0.020	1239	0.63	2.02	8.28	3.38	1.65
0.07Ti-MCM-48	0	0	0.07	0.031	1227	0.66	2.14	8.33	3.40	1.65
0.09Ti-MCM-48	0	0	0.09	0.034	978	0.55	2.27	8.23	3.36	1.58
0.01Fe-0.01Ti-MCM-48	0.01	0.005	0.01	0.007	1460	0.96	2.64	8.65	3.53	1.48
0.01Fe-0.03Ti-MCM-48	0.01	0.006	0.03	0.020	1362	0.72	2.21	8.40	3.43	1.61
0.01Fe-0.05Ti-MCM-48	0.01	0.007	0.05	0.028	1269	0.68	2.14	8.23	3.36	1.59
0.01Fe-0.07Ti-MCM-48	0.01	0.006	0.07	0.035	1049	0.58	2.21	8.13	3.32	1.52

[a] $a_0 = d_{211}(6)^{1/2}$, [b] Wall thickness = $a_0/3.0919$ – pore diameter/2, * Data were obtained from XRF.

5.4.5 SEM

Figure 5.5 shows the SEM micrographs of pure MCM-48, Fe-MCM-48, Ti-MCM-48, and Fe-Ti-MCM-48. The truncated octahedral shape of MCM-48 was shown in Fig. 5.5a. Fe-MCM-48 and Ti-MCM-48 morphologies shown in Fig. 5.5b-c had some distortion from the pure MCM-48 due to the larger size of Fe and Ti, as discussed above. Because of the existence of both Fe and Ti, bimetallic Fe-Ti-MCM-48 exhibited even more distortion in the structure. Moreover, the bimetallic crystal size decreased as the amount of Ti increased since the more ions generated many nuclei and resulted in more small growing crystal [48-49].
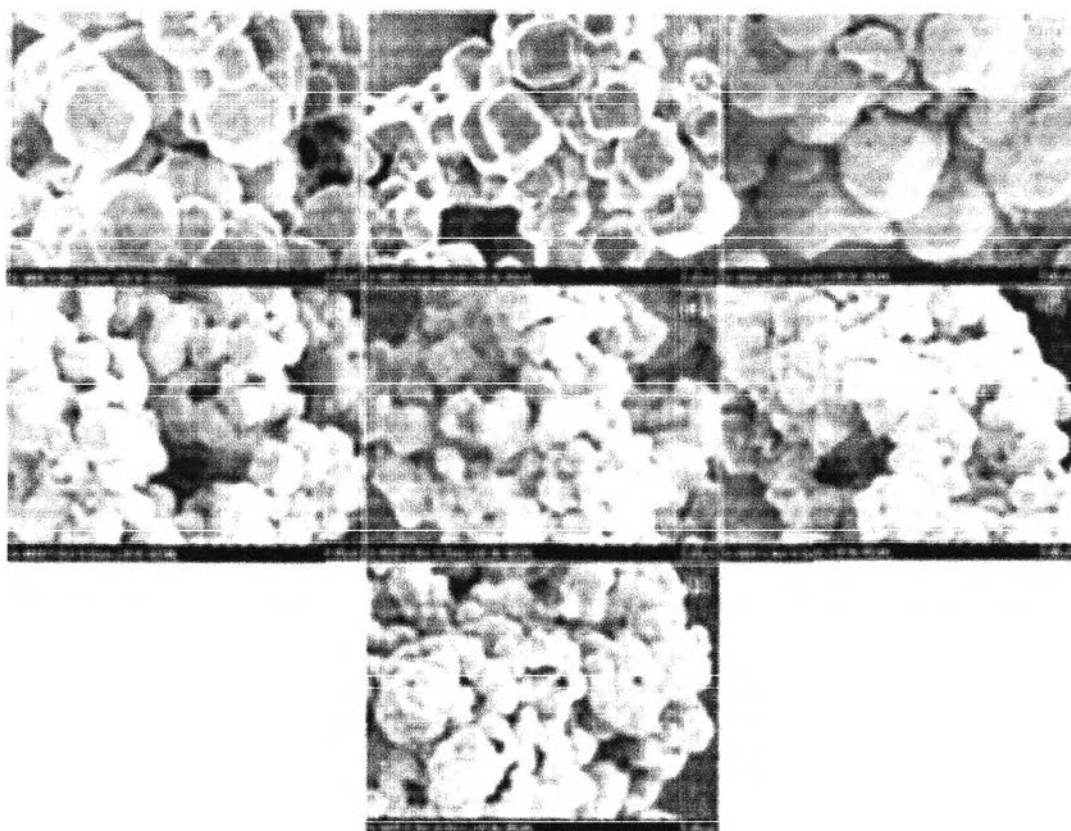
Figure 5.5 FE-SEM images of samples: (a) MCM-48; (b) 0.01Fe-MCM-48; (c) 0.01Ti-MCM-48; (d) 0.01Fe0.01Ti-MCM-48; (e) 0.01Fe0.03Ti-MCM-48; (f) 0.01Fe0.05Ti-MCM-48, and (g) 0.01Fe0.07Ti-MCM-48.

5.4.6 TEM

The structural order of 0.01Fe0.01TiMCM-48 observed by TEM indicated the projection along (100) direction [34], see Fig. 5.6a-b, showing the highly ordered cubic structure with uniform mesopores. Fortunately, the introduction of Fe and Ti atoms did not destruct the mesoporous structure.
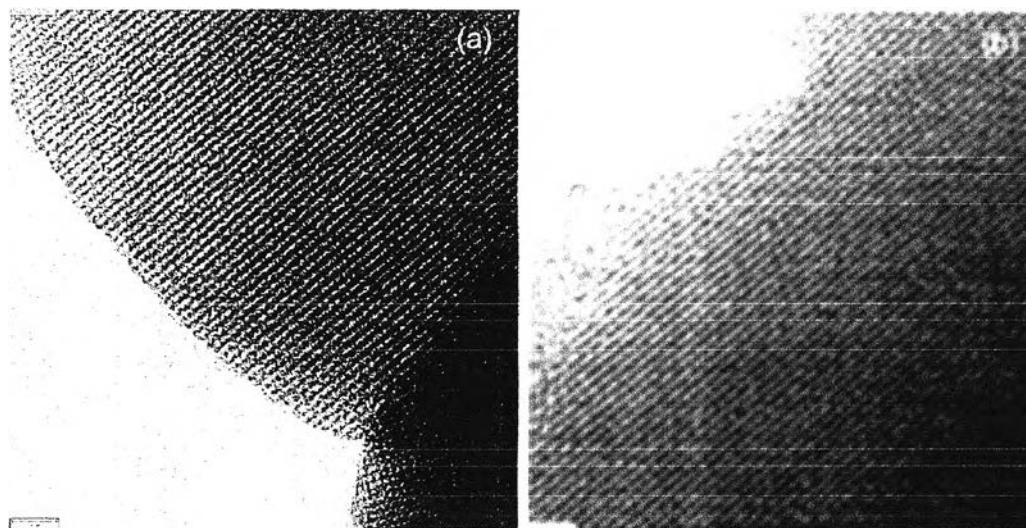

Figure 5.6 TEM images of 0.01Fe0.01TiMCM-48 along the (100) direction.

5.4.7 Hydrothermal stability

Figure 5.7 presents the XRD patterns of 0.01Fe0.01Ti-MCM-48 sample after hydrothermal treatment at 100 °C for 0, 12, 24, 36, 48, and 72. It was shown that 0.01Fe0.01Ti-MCM-48 has the characteristic peaks of {211} and {220} after 12 h treatment, but the diffraction peaks of {420} and {322} were not seen due to the distortion of the structure from the incorporation of Fe and Ti, making the sample less order. However, the diffraction peaks of {211} and {220} retained for 48 h treatment while the {211} peak still maintained after 72 h treatment. For 0.01Fe (0.03-0.07) Ti-MCM-48 and (0.03-0.09)Ti-MCM-48, the characteristic peaks disappeared after 12 h treatment (not shown) because the more amounts of the metal

incorporated resulted in the more distortion, leading to easier destruction. The XRD patterns of pure MCM-48 and 0.01Fe-MCM-48 collapsed after 48 h treatment whereas the peak of 0.01Ti-MCM-48 disappeared after 24 h treatment. In addition, they lost the diffraction {220} peak after the 12 h treatment. It revealed that the Fe-O-Si bonds and Ti-O-Si bonds have low resistance for water attack [46]. For MCM-48, the water molecule caused the hydrolysis of Si-O-Si bonds, resulting in the poor silica wall which led to the collapse of the silicate structure [50]. Of all synthesized bimetallic MCM-48, the most hydrothermal stable one is 0.01Fe0.01Ti-MCM-48. It could be suggested that the existence of extraframework titanium shielded the siloxane bonds (Si-O-Si) and obstructed the interaction with water molecules which enhanced the stability in boiling water [24]. Nevertheless, Fe-Ti-MCM-48 with 0.01Fe/Si and 0.03-0.07 Ti/Si showed the deterioration stability. There are two possible reasons supporting this situation. The first one is from both high amount of tinatium and two different types of metal atoms incorporated in the structure, resulting in the distortion and easier destruction. The other reason is from the extraframework of titania blocking the pore of MCM-48, causing the partially wall breakage and a decrease in surface area [29].
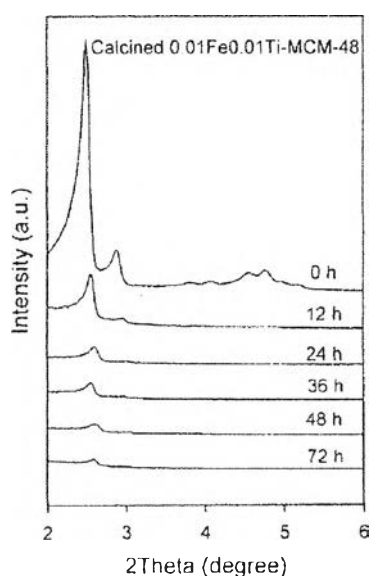
Figure 5.7 XRD patterns of 0.01Fe0.01Ti-MCM-48 after hydrothermal treatment at 100 °C for different times (0, 12, 24, 36, 48 and 72 h).

5.5 Conclusions

A series of iron and titanium incorporated MCM-48 mesoporous materials with high surface area were successfully synthesized from silatrane via sol-gel method. High iron content is unfavorable for Fe-MCM-48 formation while Ti-MCM-48 resulted in a cubic structure. The introduction of iron and titanium ions led to a decrease of Fe-Ti-MCM-48 surface area generated the extraframework. The resulting 0.01Fe0.01Ti-MCM-48 mesoporous molecular sieve has high hydrothermal stability, suitable for many applications.

5.6 Acknowledgements

5.7 References

[1]C.T. Kresge, M.E. Leonowicz, W.J. Roth, J.C. Vartuli, J.S. Beck, Nature 359 (1992) 710-712.

[2]A. Taguchi, F. Schüth, Microporous Mesoporous Mater. 77 (2005) 1-45.

[3]N.Z. Logar, V. Kaučič, Acta. Chim. Slov. 53 (2006) 117-135.

[4]V. Meynen, P. Cool, E.F. Vansant, Microporous Mesoporous Mater.125 (2009) 170-223.

[5]P. Xue, G.Z. Lu, Y.L. Guo, Y.S. Wang, Y. Guo, J. Mol. Catal. B: Enzym. 30 (2004) 75-81.

[6]I.B. Isabel, M. África, L.D. Antonio, P.P. Joaquin, V.R. Maria, Eur. J. Pharm. Sci. 26 (2005) 365-373.

[7]L.Huang, Q.L. Huang, H.N. Xiao, M. Eic, Microporous Mesoporous Mater. 111 (2008) 404-410.

[8] M. Kruk, M. Jaroniec, R. Ryoo, S.H. Joo, J. Phys. Chem. B 104 (2000) 7960-7968.

[9] C. Huo, H. Zhang, H. Zhang, H. Zhang, B. Yang, P. Zhang, Y. Wang, Inorg. Chem. 45 (2006) 4735-4742.

[10] W. Zhao, Y. Luo, P. Deng, Q. Li, Catal. Lett. 73 (2001) 2-4.

[11] M. Selvaraj, D.W. Park, C.S. Ha, Microporous Mesoporous Mater. 138 (2011) 94-101.

[12] H.T. Gomes, P. Selvam, S.E. Dapurkar, J.L. Figueiredo, J.L. Faria, Microporous Mesoporous Mater. 86 (2005) 287-294.

[13] M.S. Hamdy, G. Mul, J.C. Jansen, A. Ebaid, Z. Shan, A. R. Overweg, Th. Maschmeyer, Catal. Today 100 (2005) 255-260.

[14] W. Tanglumlert, T. Imae, T.J. White, S. Wongkasemjit, Catal. Commun. 10 (2009) 1070-1073.

[15] L.A. Cano, M. V. Cagnoli, J.F. Bengoa, A.M. Alvarez, S.G. Marchetti, J. Catal. 278 (2011) 310-320.

[16] H. Liu, G. Lu, Y. Guo, Y. Guo, J. Wang, Nanotechnology 17 (2006) 997-1003.

[17] F. Adam, J. Andas, I.Ab. Rahman, Chem. Eng. J. 165 (2010) 658-667.

[18] R. Peng, D. Zhao, N.M. Dimitrijevic, T. Rajh, R. T. Koodali, J. Phys. Chem. C 116 (2012) 1605-1613.

[19] T. Liou, B. Lai, Appl. Catal. B 115-116 (2012) 138-148.

[20] M. Popova, Á. Szegedi, P. Németh, N. Kostova, T. Tsoncheva, Catal. Commun. 10 (2008) 304-308.

[21] C.H. Rhee, J.S. Lee, Catal. Lett. 40 (1996) 261-264.

[22] F.-S. Xiao, Y. Han, Y. Yu, X. Meng, M. Yang, S. Wu, J. Am. Chem. Soc. 6 (2002) 124.

[23] L.Y. Chen, S. Jaenicke, G.K. Chuah, Microporous Mater. 12 (1997) 323-330.

[24] C. Galacho, M.M.L.R. Carrott, P.J.M. Carrott, I.P.P. Cansado, Adv. Mat. Res. 107 (2010) 63-70.

[25] D. Rath, K.M. Parida, Ind. Eng. Chem. Res. 50 (2011) 2839-2849.

[26] Y. Wu, Y. Zhang, J. Cheng, Z. Li, H. Wang, Q. Sun, B. Han, Y. Kong, Microporous Mesoporous Mater. 162 (2012) 51-59.

[27] Y. Wang, Y. Guo, G. Wang, Y. Liu, F. Wang, J. Sol-Gel Technol. 57 (2011) 185-192.

[28] Y. Kong, S. Jiang, J. Wang, S. Wang, Q. Yan, Y. Lu, Microporous Mesoporous Mater. 86 (2005) 191-197.

[29] Z. Wang, X. Ci, H. Dai, L. Yin, H. Shi, Appl. Surf. Sci. 258 (2012) 8258-8263.

[30] H. Zhang, C. Tang, C. Sun, L. Qi, F. Guo, L. Dong, Y. Chen, Microporous Mesoporous Mater. 151 (2012) 44-55.

[31] F. Gao, Y. Zhang, C. Wang, C. Wu, Y. Kong, B. Zhao, L. Dong, Y. Chen, J. Nanosci. Nanotechnol. 7 (2007) 4508-4514.

[32] Y. Zhang, F. Gao, H. Wan, C. Wu, Y. Kong, X. Wu, B. Zhao, L. Dong, Y. Chen, Microporous Mesoporous Mater. 113 (2008) 393-401.

[33] M. Popova, A. Szegedi, Z. Cherkezova-Zheleva, I. Mitov, N. Kostova, T. Tsoncheva, J. Hazard. Mater. 168 (2009) 226-232.

[34] R. Longloilert, T. Chaisuwan. A. Luengnaruemitchai. S. Wongkasemjit, J. Sol-Gel Sci. Technol. 58 (2011) 427-435.

[35] W. Charoenpinijkarn, M. Suwankruharn, B. Kesapabutr, S. Wongkasemjit, A.M. Jamieson, Eur. Polym. J. 37 (2001) 1441-1448.

[36] T. Jiang, D. Wu, J. Song, X. Zhou, Q. Zhao, M. Ji. H. Yin, Powder technol. 207 (2011) 422-427.

[37] S. Wang, Y. Shi, X. Ma, Microporous Mesoporous Mater. 156 (2012) 22-28.

[38] H. Maneesuwan, R. Longloilert, T. Chaisuwan, S. Wongkasemjit. Mater. Lett. 94 (2013) 65-68.

[39] W. Zhao, L. Kong, Y. Luo, Q. Li, Microporous Mesoporous Mater. 100 (2007) 111-117.

[40] L.M. Mahoney, Photocatalysis studies using mesporous modified V-MCM-48 Stober Synthesis, PhD thesis, Kansas State University, 2010

[41] G.D. Mihai, V. Meynen, M. Mertens, N. Bilba, P. Cool, E.F. Vansant, J. Mater. Sci. 45 (2010) 5786-5794.

[42] J. Jiao, Q. Xu, L. Li, J. Colloid Interface Sci. 316 (2007) 596-603.

[43] A. Jaroenworaluck, N. Pijarn, N. Kosachan, R. Stevens. Chem. Eng. J. 181-182 (2012) 45-55.

[44] S.K. Das, M.K. Bhunia, A. Bhaumik, Open Catal. J. 5 (2012) 56-65.

[45] D. Ji, T. Ren, L. Yan, J. Suo, Mater. Lett. 57 (2003) 4474-4477.

[46] Y. Shao, L. Wang, J. Zhang, M. Anpo, J. Phys. Chem. B 109 (2005) 20835-20841.

[47] D. Zhao, S. Budhi, A. Rodriguez, R.T. Koodali, Int. J. HydrogenEnergy 35 (2010) 5276-5283.

[48] P.G. Vekilov, Cryst. Growth Des. 10 (2010) 12.

[49] D. Kashchiev, G.M. Van Rosmalen, Cryst. Res. Technol. 38 (2003) 7-8.

[50] K.A. Koyano, T. Tatsumi, Y. Tanaka, S. Nakata, J. Phys. Chem. B 101 (1997) 436.

[51] N. Serpone, J. phys. Chem B 110 (2006) 24287-24293. R. Oleksak, W.F. Stickle, G. Herman, J. Mater. Chem. C (2015) Accepted Manuscript, DOI: 10.1039/C4TC02985B.

[52] R. Oleksak, W.F. Stickle, G. Herman, J. Mater. Chem. C (2015) Accepted Manuscript, DOI: 10.1039/C4TC02985B.

[53] S. Artkla, W. Choi, J. Wittayakun, EnvironmentAsia 1 (2009) 41-48.